Shap. Mem. Superelasticity
https://doi.org/10.1007/s40830-025-00554-9

ORIGINAL RESEARCH ARTICLE

High-Durability Nitinol for Medical Devices: A 100 Million-Cycle Bending Fatigue Characterization Study

Maximilien E. Launey[1] · Sean M. Pelton[1] · Harjot Gill[1] · Payman Saffari[2] · Andreas Keck[3] · Jochen Ulmer[3] · Pawel Czaja[4,5] · Andrew Barnum[6] · Robert Sinclair[5] · Alan R. Pelton[1,5]

Received: 28 March 2025 / Revised: 16 June 2025 / Accepted: 24 June 2025

Abstract This study investigates the bending fatigue performance of Vacuum Arc Remelted/Electron Beam Refined (VAR/EBR) Nitinol for cardiovascular applications. Diamond-shaped fatigue specimens were manufactured from ultra-clean VAR/EBR Nitinol tubing with inclusion sizes below 10 µm and tested under physiologically relevant conditions to 100 million cycles. Testing included multiple combinations of mean strains (0–7%) and strain amplitudes (0.75–2.50%) to simulate in vivo conditions for cardiovascular devices. Results demonstrate that VAR/EBR Nitinol exhibits as high as 275% improvement in 10^8-cycle Fatigue Strain Limit (FSL) compared to conventional VAR Nitinol at mean strains between 3 and 5%. The FSL behavior shows three distinct strain regimes: increasing FSL with mean strains from 0 to 3%, plateau between 3 and 5%, and decreasing FSL beyond 5%. Analysis confirms the critical impact of limiting inclusion size below the theoretical critical small crack length of 10 µm, where fatigue performance becomes dictated by cyclic stress/strain rather than flaw size. Advanced (S)TEM imaging of the fatigue specimens provides evidence that advanced thermomechanical processing leads to stable microstructures to enhance fatigue response up to 10^8 fatigue cycles.

Keywords Fatigue · Cyclic stability · NiTi · Intrinsic inclusions

Introduction

Nitinol, a nearly equiatomic nickel-titanium alloy, is a prominent material in biomedical engineering due to its exceptional shape memory properties, superelasticity, and biocompatibility [1]. The material's capacity for recoverable strain accommodation up to 8% through temperature- and stress-induced martensitic transformations has enabled significant advances in minimally invasive medical procedures. Within the last decade, significant technological advancements in the melting, processing, manufacturing, and modeling of Nitinol have allowed it to emerge as a material of choice for critical and challenging applications such as Class III life-supporting and life-sustaining medical devices.

The durability requirements for Nitinol cardiovascular devices, including heart valve frames, are governed by stringent international standards, as well as guidance from regulatory bodies, including ISO 5840 [2], FDA Guidance Document [3], and various ASTM specifications [4–7]. Recent regulatory developments emphasized comprehensive fatigue analysis protocols that encompass anatomical boundary conditions, stress/strain analysis, material fatigue strength

This article is an invited paper selected from presentations at the Shape Memory and Superelastic Technologies Conference and Exposition 2024, held May 6–10, 2024, in Cascais, Portugal, and has been expanded from the original presentation. The issue was organized by Dr. Parikshith Kumar, W. L. Gore & Associates, Inc., Prof. William LePage, University of Tulsa, and Dr. Harshad Paranjape, Confluent Medical Technologies.

✉ Alan R. Pelton
Alan.Pelton@g-rau.com

1 G. RAU Inc, Scotts Valley, CA, USA

2 Engage Medical Device Services Inc, Newport Beach, CA, USA

3 Euroflex GmbH, Pforzheim, Germany

4 Institute of Metallurgy and Materials Science, Polish Academy of Sciences, Kraków, Poland

5 Department of Materials Science and Engineering, Stanford University, Stanford, CA, USA

6 Stanford Nano Shared Facilities, Stanford University, Stanford, CA, USA

Published online: 29 July 2025

assessment, component fatigue demonstration, and safety factor calculations. In regulating prosthetic heart valves, the United States Food and Drug Administration (USFDA) challenges device manufacturers to identify the proper boundary conditions for in vitro testing, and with the performance of new materials such as Nitinol in the dynamic environment of heart valve implantation sites [8]. The regulatory framework for cardiovascular devices necessitates fatigue resistance verification for extended service lives: 400 M cycles (10 years) per ISO 5840 and 600 M cycles (15 years) per USFDA guidelines.

Recent fatigue studies [9, 10] expanded investigation parameters to include multiple mean strains and strain amplitudes, that use coupons extracted from the device or surrogate specimens, including, but not limited to, diamond-, Z-, or C-shaped manufactured from tubing, wire or sheet with pre-strain conditions that mimic cardiovascular implant applications. These investigations identified several strategies to enhance in vivo fatigue resistance, namely:

i. Optimization of pre-strain (crimp strain) parameters
ii. Control of mean strain (oversizing) conditions
iii. Stress–strain (energy) consideration
iv. Optimization of material, including thermomechanical processing (e.g., reduction of grain size) and micropurity (reduction of inclusion size)

i. Optimization of Pre-Strain

Research results have demonstrated (see for example, [9, 10], and references therein) that significant improvements in fatigue performance may be realized through pre-strain, with up to 180% increase in fatigue strain limits through pre-strain optimization. The effects of pre-strain or related effects of "training" indicate that there are optimal combinations of thermo-mechanical processing with subsequent pre-straining (straining prior to application cycling) that tend to stabilize the microstructures and textures for temperature, stress, or strain cycling. The data clearly show that, for a constant mean strain (hence a constant cyclic modulus), increases in the Fatigue Strain Limit (FSL) are related to an increase in the stress hysteresis with increasing pre-strain as predicted by the Hooke's law. These experimental results are consistent with the metallurgical effects that involve selective martensite variant formation, plasticity, texture changes and resultant residual stresses [11–15].

ii. Control of Mean Strain

Several studies addressed the effects of mean strain on the fatigue behavior of superelastic Nitinol, all of which have been summarized and discussed recently [9, 16]. Tabanli, et al. [17, 18] were the first to discuss this topic and hypothesized that short fatigue lives are associated with strain-driven phase transformations, whereas long fatigue lives require cycling within a single-phase regime. This hypothesis was later reinforced by others in fatigue testing of Nitinol stent subcomponents [19] and thermomechanically processed wires [20]. It is now well established that mechanical cycling in the two-phase region results in grains with B2 austenite and grains with stress-induced B19' martensite and that the relative volume fractions of these two phases changes with testing conditions (i.e., mean strain). Furthermore, these two phases accommodate different amounts of strain due to the applied deformations (see, for example, [11, 21–23]). For example, Catoor, et al. demonstrated with DIC analysis of tension-tension fatigue of Nitinol sheet that austenite grains accommodated a maximum of ~ 1% strain whereas the martensite grains had up to ~ 6% strain [24]. The net effect in the change in global mean strain results in a change in the effective modulus and stress amplitude [10].

Uniaxial fatigue data indicated that the fatigue threshold under tension–tension conditions is the strain amplitude that separates linear austenite cyclic loading and stress-induced martensite transformation (SIMT) loading [10, 24]. Launey et al. [10] investigated mean strains within the mixed-phase (austenite–martensite) region on the unloading plateau after 6% pre-strain such that $\varepsilon_{fA} < \varepsilon_m < \varepsilon_{sA}$.[1] (i.e., 1%, 3%, and 4.5% mean strain), and reported up to 175% enhancement of the FSL through an increase in mean strain. The investigation showed a decrease in the cyclic modulus with an increase in mean strain likely a result of an increased volume fraction of martensite within the stressed volume. In the case of displacement- or strain-controlled tests, cyclic deformation is accommodated over higher strain amplitude as the mean strain increases and cyclic modulus decreases.

Pelton et al. [25] investigated the effects of mean strain and strain amplitude on thermomechanically processed Nitinol diamond-shaped test coupons representative of the stent manufacturing processes. The investigators constructed a 10^7-cycle strain-life diagram for a wide range of combinations of mean strain and strain amplitudes. The data indicated that there is a minimum in the fatigue life in regions at boundaries between the phases (e.g., in the range of ~ 0.5 to 1.5% mean strains where phase transformation initiates or ~ 6% where the stress-induced martensitic transformation saturates), and that the fatigue life remains relatively independent of mean strain within the plateau region until new variants of martensite are activated at higher stresses and plastic flow increases. Other investigations also indicate similar effects of mean strain on superelastic fatigue behavior [19, 20, 26].

[1] ε_{fA} is defined as the strain that corresponds to the Austenite Finish on the unloading curve; ε_m is the mean strain; ε_{sA} is defined as the strain that corresponds to the Austenite Start on the unloading curve.

Cao et al. [27] investigated the influence of mean strain on the high cycle fatigue (> 10^8 cycles) of C-shaped Nitinol surrogate specimens. Their investigation describes FSL behavior in two distinct strain regimes: (i) a decrease in FSL with mean strain up to 3%, and (ii) a non-sensitivity to mean strains between 3 and 8%. Cao et al. further indicates that ultra-high cycle fatigue (UHCF) failures were observed at high cycle counts (> 10^7 cycles) without providing microstructural mechanisms to explain these phenomena. Interestingly, these are the only investigators to report such fatigue behavior in superelastic Nitinol.

Recently, Weaver et al. investigated high frequency (167–400 Hz) and ultra-high cycle rotary bend fatigue (mean strain of 0% or R = − 1) of commercial grade VIM/VAR Nitinol wire to 1 billion cycles and beyond [28]. The authors reported that superelastic Nitinol exhibits a bimodal fatigue life, i.e., a short life up to ~ 2×10^5 life with cyclic phase transformation and UHCF life with failures that start to occur frequently beyond 6×10^7 cycles. A follow up study by Roiko, et al. [29] highlighted a new feature observable in UHCF fractures of Nitinol that is best described as a thumbnail shaped smooth area, termed as the region of reduced roughness (RRR), surrounding the inclusion/void that initiated the fatigue crack. The RRR appears to grow with the cycle count and is observable only on specimens subjected to at least 10^7 cycles. Crack growth from small inclusions associated with low stress intensity thresholds for small crack growth, $\Delta K_{th,\ small\ crack}$, may provide a means to estimate UHCF fractures, although further refinement, including the effects of mean stresses/strains, is required.

iii. Stress-Strain (Energy) Consideration

Energy-based prediction models for Nitinol that rely on the dissipated energy at the stabilized cycle have been recently proposed [10, 30, 31]. The energy-based prediction parameter indicates the tension–tension fatigue threshold is the strain amplitude that separates linear austenite cyclic loading and SIMT cyclic loading. The dissipated energy quickly rises once the maximum stress of the loading cycles reaches the upper plateau stress of the material. In the case of linear cyclic regime, high cycle life up to at least 10^7 cycles is likely as the dissipated energy (i.e., hysteresis area) is close to zero. Conversely, fatigue fractures are to be expected when operating into the SIMT regime. Based on a limited set of data, the energy-based prediction model that relies on the dissipated energy appears to be a reasonably good prediction tool for fatigue life prediction of Nitinol under tension-tension conditions. Further investigations are required to validate the approach and for use with other deformation modes such as cyclic bending (Mode I/II).

iv. Material Micropurity

The effects of inclusion size and area fraction on fatigue results reported in [32, 33] afford great insights into the potential benefits of high-purity microstructures (e.g., smaller inclusion size, lower inclusion area fraction). The development of "ultraclean" Nitinol variants, characterized by reduced non-metallic inclusion (NMI) size and content is a significant metallurgical advancement. These materials maintain compliance with ASTM F2063[2] specifications while achieving superior microstructural characteristics. The primary focus has been to minimize Titanium Oxide ($Ti_4Ni_2O_x$) and Titanium Carbide (TiC) inclusions that act as fracture initiation sites under cyclic loading conditions. Recent investigations demonstrated significant improvements in fatigue performance through advanced processing techniques, particularly Electron Beam Refining (EBR) technology. Several recent investigations were conducted to document the fatigue response of VAR/EBR[3] Nitinol under a variety of test conditions [33, 34]. In these studies, fatigue specimens were manufactured from 10 mm OD × 0.53 mm WT Nitinol tubing from VAR II, VIM/VAR II, and VAR/EBR ingots.[3] As reported in previous fatigue studies [32, 33], VAR II and VIM/VAR II Nitinol have comparable 10^7-cycle fatigue behavior. VAR/EBR Nitinol showed a remarkable ~ 2 × improvement in the FSL over VAR II and VIM/VAR II Nitinol under bending fatigue with 6% pre-strain and 5% mean strain. For example, to achieve a 0% probability of fracture to 10^7 cycles (i.e., 100% survival to 10^7 cycles), VAR II and VIM/VAR II indicate a maximum bending strain amplitude of ~ 1%, compared with ~ 2% bending strain amplitude for VAR/EBR Nitinol.

The present investigation extends the 10^7-cycle fatigue data for VAR/EBR Nitinol that was conducted under one mean strain [33, 34], and focuses on the effects of a combination of multiple mean strains and strain amplitudes on the bending fatigue behavior of VAR/EBR Nitinol to 10^8 cycles.

Materials and Methods

VAR/EBR Nitinol Tubing

EBR is a processing technique for the refinement of metals and alloys that uses electron beam melting under high vacuum. This process is the industry standard for the production of refractory and reactive metals (e.g., tantalum, niobium, molybdenum, tungsten, vanadium, hafnium, zirconium, and

[2] Current ASTM standards specify maximum NMI dimensions of 39.0 µm and area fractions of 2.8% in mill products.

[3] VAR: Vacuum Arc Remelt; VIM: Vacuum Induction Melt; VIM/VAR: Combination of VIM and VAR processes; VAR II: Low Inclusion (Gen II) Vacuum Arc Remelt; VIM/VAR II: Low Inclusion (Gen II) VIM/VAR; VAR/EBR: Electron Beam Refining of VAR material.

titanium) and their alloys [35]. EBR enables control of the formation of phases that depend on temperature gradients during solidification. With regard to production of the VAR/EBR Nitinol discussed in this paper, a VAR ingot is produced with a conventional vacuum arc melting method, and is then converted to bars with typical hot working processes that include press forging and rotary forging. These bars are then gun drilled to produce "tube hollows" that are subsequently subjected to an additional "in situ" EBR melting at G.RAU GmbH (Pforzheim, Germany). The EBR process is carried out under high vacuum to minimize exposure to oxygen during processing. Furthermore, a crucible-free process is used for the refinement so that there is no contamination as is observed in other melt methods (e.g., carbon contamination from graphite crucibles with VIM). The full characterization of chemistry, grain size, inclusion size and area fraction, mechanical properties, and transformation temperatures are evaluated in the annealed hot-worked EBR state in accord with ASTM F2063 [4]. Two development VAR/EBR tubing lots from two different VAR ingots were evaluated for the current investigation with slightly different thermomechanical processing. Given that these processing conditions were nearly identical the fatigue results will be pooled for this paper.

The hot-worked and annealed EBR tubing lots had an average austenite start transformation temperature, A_s, of − 21 and − 28 °C as measured by DSC [5], maximum inclusion sizes of 6.0 and 7.4 µm, and inclusion areas of 0.38 and 0.43% [4]. The VAR/EBR $Ni_{50.8}Ti_{49.2}$ (at.%) tubes were drawn at G.RAU GmbH with two slightly different sets of cold work and stress-relief process steps to 7.00 mm outer diameter (OD) and 0.50 mm wall thickness (WT). All tubes were subsequently straightened in a horizontal furnace to achieve as close to identical thermal and mechanical properties as possible, including upper and lower plateau stresses (Table 1).

Test Coupon Processing

Diamond-shaped stent surrogate test specimens were fabricated from the tubes with the struts aligned parallel to the tubing longitudinal axis via ultra short pulse laser manufacturing. The resulting diamond structures were then expanded in two steps to their final shape (Figs. 1 and 2a) for a total of 6 min processing time at 505 °C. The shape-set diamond test specimens were electropolished to ensure uniform surface smoothness and to eliminate surface oxides as well as any heat affected zone material. All diamond specimens were manufactured by Admedes GmbH (Pforzheim, Germany) with a total of eight manufacturing lots from the two VAR/EBR tube lots. All finished diamond-shaped specimens had an A_f temperature of 20 ± 3 °C as measured by DSC. Post-electropolishing, the fatigue test coupons had nominal dimensions of 7.57 ± 0.10 mm diamond height, 21.7 ± 0.1 mm width, and 0.460 ± 0.030 mm wall thickness. Strut widths were 0.285 ± 0.015 mm except at the tips of the diamond where the dimension was increased to 0.356 ± 0.020 mm. The eight locations of the double-diamond specimen will have similar fatigue stresses/strains, and therefore fracture may occur at any of these locations. As such, it is critical to ensure that each strut meets the dimensional requirements defined above. 100% dimensional inspection including 16 measurement locations per diamond coupon was performed. The diamond pair is considered as a single test article for the fatigue test; i.e., a fracture at any location is considered as a device fracture.

Fig. 1 As as-manufactured "double diamond" Nitinol coupon specimen

Mechanical and Thermal Properties

Tensile dogbone specimens were processed from both lots of tubing and were subjected to identical heat treatments

Table 1 Engineering mechanical properties from two material lots of VAR/EBR tubing that were heat treated to simulate coupon processing conditions

Material lot	Austenite modulus (GPa)	Upper plateau stress (MPa)	Lower plateau stress (MPa)	Permanent set (%)	Uniform elongation (%)	Ultimate tensile stress (MPa)
1	67.0 ± 0.4	400.6 ± 4.4	166.1 ± 5.2	0.07 ± 0.04	15.6 ± 0.4	1199.7 ± 8.8
2	71.1 ± 9.4	394.7 ± 15.4	138.9 ± 7.6	0.03 ± 0.05	12.7 ± 0.3	1185.8 ± 18.6

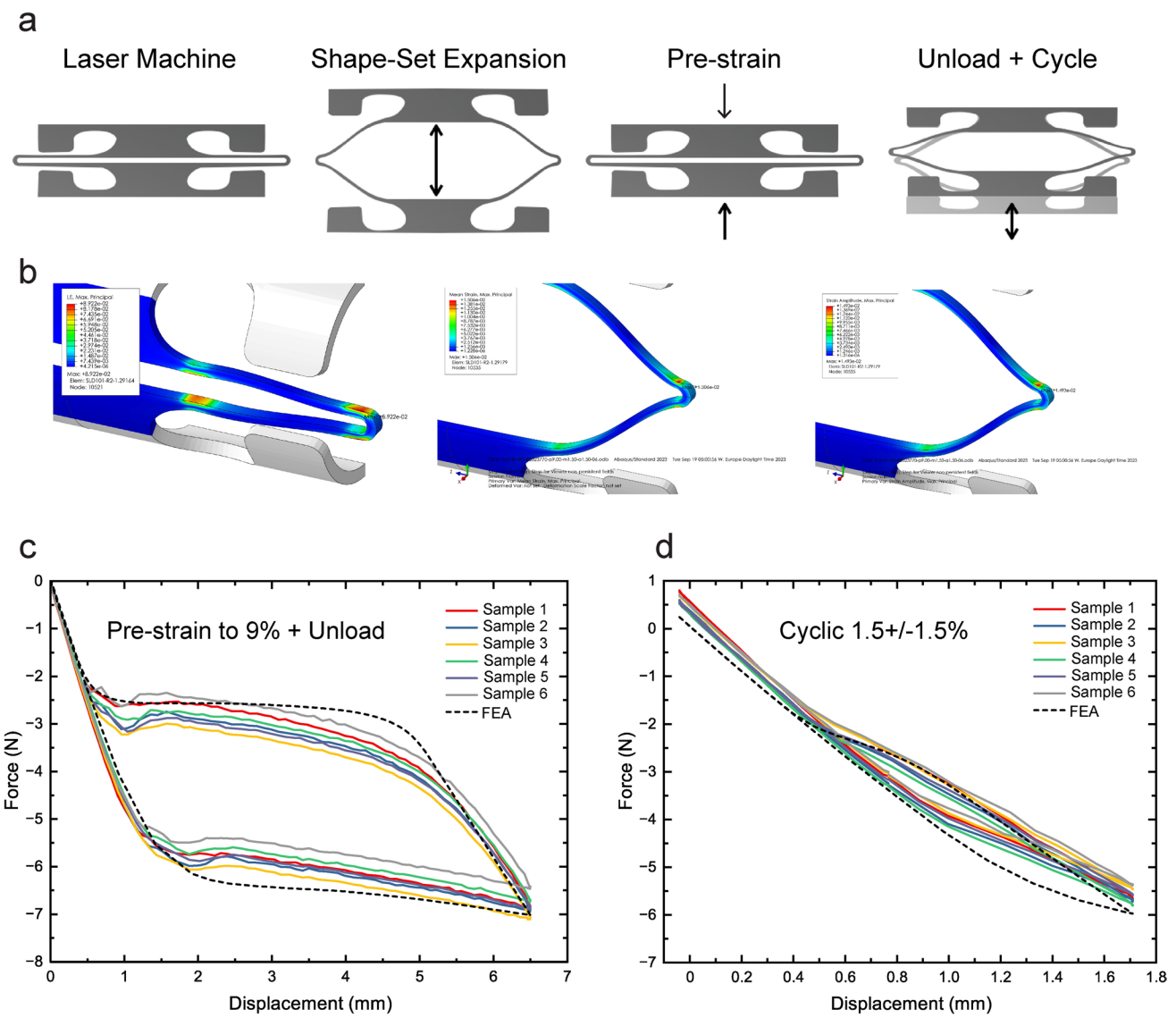

Fig. 2 **a** Manufacturing (laser machining and shape-set expansion) and loading history (pre-straining and cyclic loading around a mean strain/stress) of a diamond coupon. **b** FEA simulation of a diamond coupon loaded at (left) 9% pre-strain, (middle) mean strain of 1.5%, and (right) strain amplitude of 1.5%. **c** Force displacement data obtained from benchtop and FEA for a (c) pre-strain of 9% and **d** cyclic strain loading of 1.50 ± 1.50%

and surface finish as the diamond coupons as discussed in the previous section. Tensile testing was conducted in accord with ASTM F2516 [36] at 37°C with an extensometer to record strain with the highest possible accuracy. The true stress–strain curves of the dogbones processed from both tubing lots are provided in Fig. 3a and the engineering mechanical properties extracted from these tests are summarized in Table 1. The DSC thermal traces in Fig. 3b and c compare the transformation temperatures of the tensile dogbone and corresponding diamond coupon specimens manufactured from the two lots of VAR/EBR tubing.

Finite Element Analysis

A diamond surrogate specimen is advantageous to simulate physiologically relevant loading conditions (e.g., pulsatile loading) of cardiovascular implants as it allows for bending deformations at the specimen apices from axial displacement of a mechanical testing system. A schematic loading sequence is shown in Fig. 2a that provides axial compression to the as-manufactured diamond specimen to the relevant crimp stress/strain applied to the device, and then cycled at the mean stress/strain ± stress/strain amplitude on the unloading plateau.

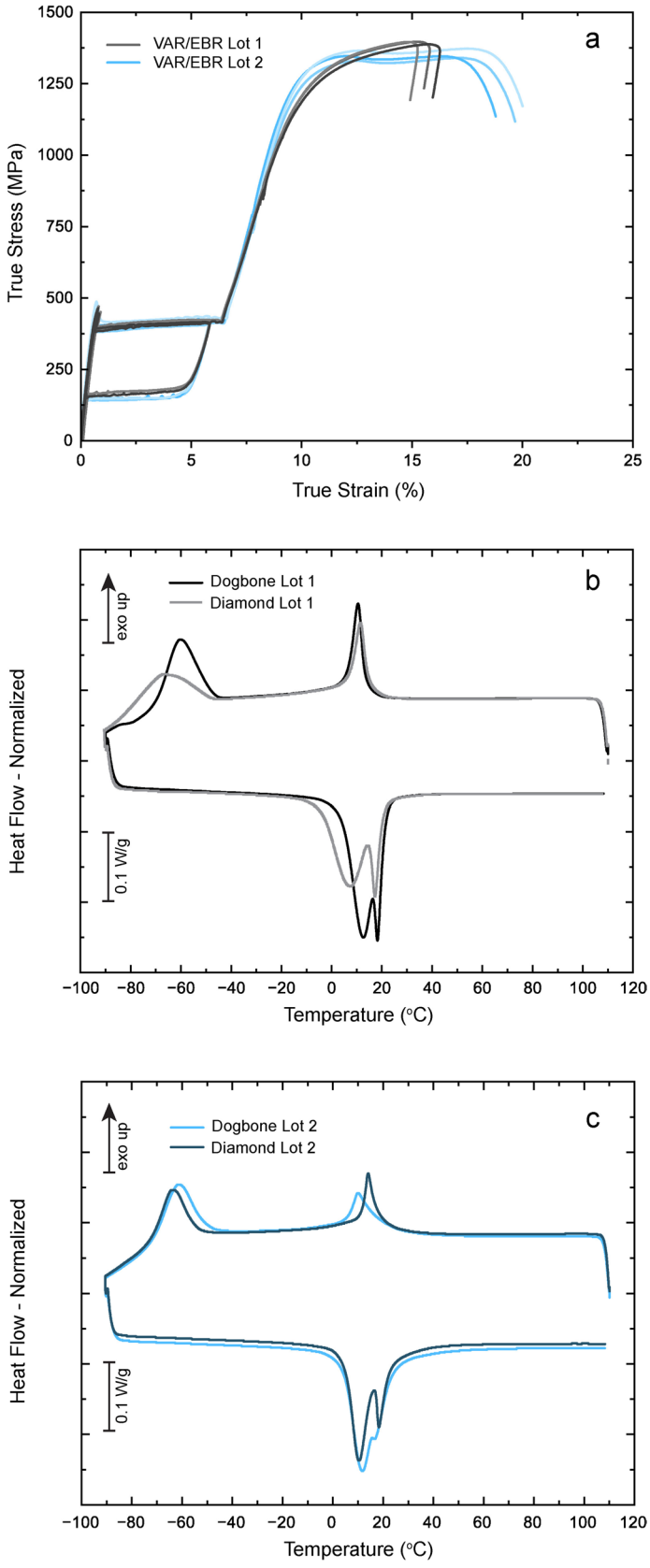

Fig. 3 **a** True stress-strain tensile curve of dogbones from VAR/EBR tube Lot 1 and Lot 2 representative of the mechanical properties of the diamond coupon specimens. DSC thermal traces of a dogbone and diamond coupon specimen manufactured from VAR/EBR **b** tube Lot 1, and **c** Lot 2 that show equivalent thermal characteristics

Finite element analysis (FEA) was conducted by Engage Medical Device Services (Newport Beach, CA USA) to estimate parameters such as internal stresses, strains and deformation patterns due to applied external forces and boundary conditions for the Nitinol bending fatigue specimens. These analyses used a FEA methodology to document strain levels experienced throughout manufacturing, crimp, and simulated in vitro cyclic loading (Fig. 2b). FEA was conducted on the fatigue test specimens in accordance with the guidelines from ASTM F2514 (Finite Element Analysis (FEA) of Metallic Vascular Stents Subjected to Uniform Radial Loading [37]), and the FDA guidance (Reporting of Computational Modeling Studies in Medical Device Submissions [38]). The model was also used in the diamond shape setting process. A mesh density of 12 × 12 (12 elements across strut width and wall thickness), based on the results of a mesh convergence study, was used for the diamond fatigue investigation. Pre-processing, post-processing, and analysis were conducted with Abaqus/CAE and Abaqus/Standard 2023 (Dassault Systèmes SIMULIA Corp, Providence, RI, USA) on a Windows 10 environment, with a multi-core Xeon processor server. Modeling of Nitinol was in accordance with "UMAT for Superelasticity of Shape Memory Alloys" included with this version of Abaqus solver. Although the tensile curves from the two VAR/EBR tube lots are comparable (Table 1, Fig. 3a), separate FEA analyses were conducted to determine if there were any significant differences between the two manufactured tube lots. Per industry conventions for superelastic Nitinol, the mean tensile curve was selected from each tube lot (N = 6 tensile tests per tubing lot) input for the FEA UMATs. Table 2 summarizes the resulting FEA UMAT parameters that were used in this investigation. By convention, the compressive plateau stresses were set to be 1.5 times greater than the tensile plateau stresses and Poisson's ratio was set to 0.33.

Validation and verification activities were conducted to examine the credibility of the FEA models developed as part of this study. Model validation of the FEA simulation included comparison against the force–displacement data from the diamond fatigue coupon when loaded under

Table 2 Superelasticity UMAT parameters for VAR/EBR Nitinol tube manufacturing lots 1 and 2

Superelasticity UMAT Parameters	Material Lot 1	Material Lot 2
Austenite Elasticity, E_A (MPa)	65000	61290
Austenite Poisson's Ratio, ν_A	0.33	0.33
Martensite Elasticity, E_M (MPa)	31111	25316
Martensite Poisson's Ratio, ν_M	0.33	0.33
Transformation Strain, ε^L	0.0525	0.0442
Start Transformation Loading, σ_L^S (MPa)	390	380
End Transformation Loading, σ_L^E (MPa)	420	400
Reference Temperature (°C)	37	37
Start Transformation Unloading, σ_U^S (MPa)	155	180
End Transformation Unloading, σ_U^E (MPa)	135	150
Start Transform Stress Compression, σ_{CL}^S (MPa)	585	570
Number of Stress-Strain Pairs	8	7
Stress in Yield Curve, σ_1^P (MPa)	960	900
Strain in Yield Curve, ε_1 (MPa)	0.085	0.08
Stress in Yield Curve, σ_2^P (MPa)	1090	1110
Strain in Yield Curve, ε_2 (MPa)	0.09	0.09
Stress in Yield Curve, σ_3^P (MPa)	1170	1240
Strain in Yield Curve, ε_3 (MPa)	0.095	0.1
Stress in Yield Curve, σ_4^P (MPa)	1250	1320
Strain in Yield Curve, ε_4 (MPa)	0.101	0.11
Stress in Yield Curve, σ_5^P (MPa)	1300	1390
Strain in Yield Curve, ε_5 (MPa)	0.109	0.13
Stress in Yield Curve, σ_6^P (MPa)	1330	1450
Strain in Yield Curve, ε_6 (MPa)	0.121	0.16
Stress in Yield Curve, σ_7^P (MPa)	1340	1470
Strain in Yield Curve, ε_7 (MPa)	0.133	0.18
Stress in Yield Curve, σ_8^P (MPa)	1345	
Strain in Yield Curve, ε_8 (MPa)	0.142	

each target pre-strain and cyclic displacement condition. For example, Fig. 2c shows the force–displacement data obtained from FEA and the benchtop data for a 9% bending pre-strain and unload. Figure 2d illustrates the cyclic force–displacement data obtained from FEA and the benchtop data for a 1.50 ± 1.50% condition.

Fatigue Testing

Fatigue testing of the diamond-shaped bending fatigue test specimens was performed with Instron (Norwood, MA USA) Electropuls 3000 equipment with 12–16 test stations at G.RAU Inc. (Scotts Valley, CA USA); each station had a calibrated force transducer rated for dynamic forces. Displacement control conditions were used for the testing whereby calibrated FEA provided the displacements associated with the initial pre-strain (9%) and variable mean strains (0–7%) and strain amplitudes (0.75–2.50%). Fatigue testing was done in 37°C deionized water at a frequency of 18–26 Hz, that depended on the displacement amplitudes. Continuous force–displacement hysteresis data were collected and stored for the 10^8 cycle tests for each specimen and each condition. Three to nine specimens from both tubing lots and different diamond manufacturing lots were tested. Specimens were cycled either until fracture occurred or 10^8 cycles run out. All fractures were examined with LOM and SEM. Three diamond struts fractured at locations that differed from the FEA-predicted "hot spots"; all three of these fractures occurred under conditions of 7% mean strain and ≥ 1.5% strain amplitude.

Microstructure Analysis

Longitudinal and transverse metallographic sections of the finished diamond coupons were prepared and examined by optical microscopy (Keyence VHX-7000) and scanning electron microscopy (FEI Quanta 200 FEG) for microstructural characterization. Sections were prepared in standard epoxy mounts and polished down to a 0.5 µm diamond suspension. Final polishing was done with a vibratory polisher with 0.02 µm colloidal silica suspension. The metallographic microstructure was revealed optically by use of a standard tint etch solution. SEM metallography was performed in the backscattered electron (BSE) mode with no etchants in order as to not modify the size or appearance of the inclusions.

Advanced (scanning) transmission electron microscopy, (S)TEM, techniques were used at the Stanford Nano Shared Facilities to investigate the microstructural modifications during the device simulation processes. Specifically, specimen lamella from diamond struts from tension "hot spot" regions were prepared with FEI Helios NanoLab 600i Dual-Beam (with Ga^+) and FEI Hydra Plasma Focused Ion Beam (with Xe^+) For this current investigation a microstructural comparison was conducted of three conditions: (1) fully processed, untested diamond specimens; (2) diamonds that were subjected to 9% pre-strain and unload; and (3) diamonds that were fatigue cycled to 10^8 cycles survival at 9% pre-strain, 3% mean strain, and 2% strain amplitude. Microstructural investigations were performed on Thermo Fisher Scientific Titan and Spectra instruments at an accelerating potential of 300 kV. Survey images at low magnifications (< 10,000 X) were obtained to determine the overall microstructures. (S) TEM annular dark field imaging with a convergence angle of 8.6 mrad and a range of camera lengths at various magnifications as well as nanodiffraction methods were used to reveal the microstructures and phases [39].

Results

Results from the microstructure analysis of the VAR/EBR material are provided in Figs. 4 and 5. The optical metallographic images of a representative finished diamond coupon in the transverse and longitudinal directions are illustrated with light optical metallography (Fig. 4a and b, respectively). Figure 4c and d show cross section SEM backscattered images in the (c) longitudinal and (d) transverse orientation of a finished diamond coupon. Diamonds manufactured from tube lots 1 and 2 display similar microstructures with an average longitudinal grain size of ~ 32 µm and transverse grain size of ~ 15 µm. The maximum inclusion size in either longitudinal or transverse orientation was found to be less than 10µm. A detailed inclusion analysis including maximum inclusion size and extreme value of VAR/EBR material will be presented in a subsequent manuscript (Pelton, et al. in preparation 2025).

Intrinsic microstructural parameters (e.g., grain size, grain orientation, inclusion size and type, and precipitation reactions) affect the fatigue behavior of superelastic Nitinol as discussed in earlier publications [40–43]. These microstructural features are best observed with transmission electron microscopy techniques such as those afforded by modern instruments with high resolution TEM and (S) TEM imaging, nanodiffraction, and compositional modes. (S)TEM images from the as-manufactured, Fig. 5(a), 9% pre-strain and unload, Fig. 5(b), and 9% pre-strain and unload to 3% mean strain plus 2% strain amplitude to 10^8 cycles Fig. 5(c) are presented. These Annular Dark Field (ADF) images [44] were obtained with a beam convergence angle of 8.6 mrad and ADF collection angle up to 37 mrad that includes multiples of the low-angle [100] and [110] B2 reciprocal lattice diffraction vectors (e.g., $3g_{110}$). These dark field imaging conditions are ideal to reveal the presence of lattice defects, including grain boundaries, dislocations, as well as martensite twins. A comparison of these three processing conditions in Fig. 5 indicates that

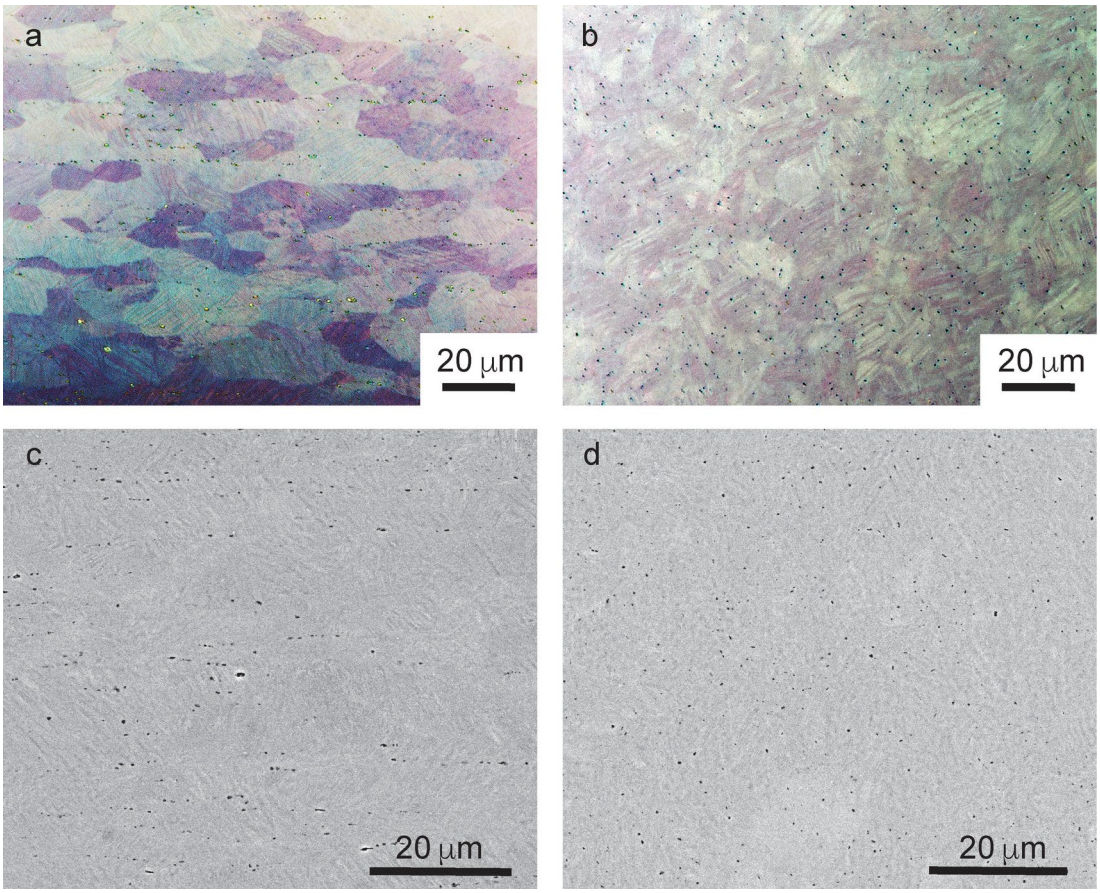

Fig. 4 Microstructures of the VAR/EBR Nitinol. Optical metallographic images of the finished diamond coupons manufactured from Lot 1 in the **a** longitudinal and **b** transverse orientation. SEM back-scattered images in the **c** longitudinal and **d** transverse orientation of a diamond coupon specimen

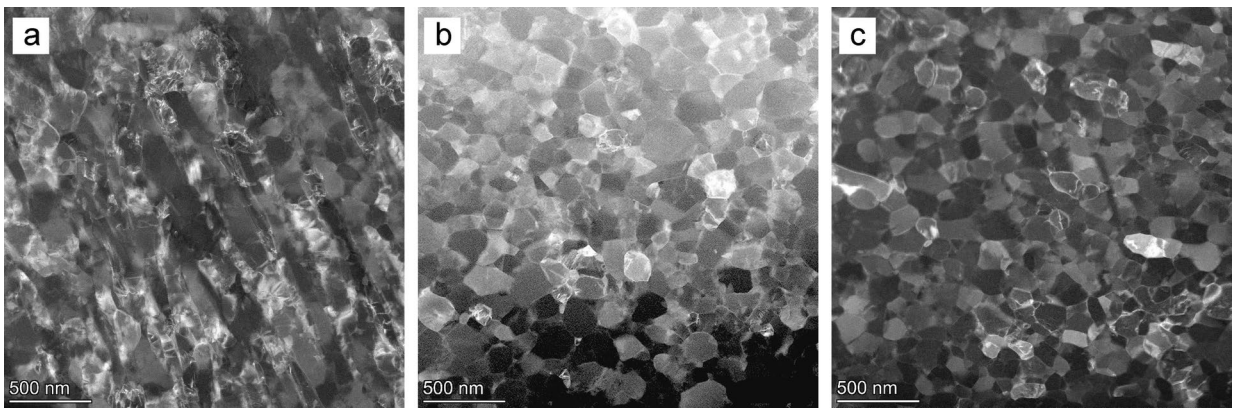

Fig. 5 (S)TEM Annular Dark Field images of microstructures of the VAR/EBR Nitinol. **a** As-manufactured condition, **b** 9% pre-strain and unload, **c** 9% pre-strain and unload to 3% mean strain plus 2% strain amplitude to 10^8 cycles. The mean grain size is ~ 150nm with low density of dislocations. These images are typical of partially recrystallized Nitinol microstructures with some regions that exhibit grain elongation **a** where other regions have a more equiaxed grain structure as exemplified in (**b** and **c**)

the microstructure primarily consists of nominally equiaxed partially recrystallized grains with an average size of ~ 150 nm with relatively low density of dislocations. Each specimen examined also had regions of slightly elongated grains, as shown for example, in Fig. 5(a). These elongated grains did not necessarily align with the drawing

direction and indicate that full recrystallization had not occurred with the processing parameters used to manufacture these diamond coupons. Surprisingly, these images reveal that the grains remain relatively free from dislocation generation even after strain excursions to 9% (Fig. 5b) and crimp plus fatigue cycling to 10^8 cycles (Fig. 5c).

The 10^8-cycle bending fatigue test results for the VAR/EBR Nitinol conducted under a pre-strain of 9% and a combination of multiple mean strains and strain amplitudes is provided in Table 3. Nineteen strain conditions were tested that resulted in a total of 123 specimens processed from the two VAR/EBR tubing lots and eight component manufacturing lots. There were no statistical differences in the fatigue results from the two VAR/EBR tubing lots; therefore, the fatigue results were pooled. Fatigue data are graphed in Fig. 6 with a conventional Nitinol FSL diagram with data plotted as a function of mean strain (abscissa) and strain amplitude (ordinate). The FSL is defined here as the 10^8 cycle fatigue strain limit at the strain amplitude where all samples survived 10^8 cycles. The circles are conditions that survived the 10^8 cycles, whereas the cross symbols indicate conditions that resulted in at least one fracture prior to 10^8 cycles. The dotted line is a visual indicator of the resultant 10^8-cycle FSL. By way of comparison, the black line illustrates previously published 10^7-cycle FSL diagram from VAR Nitinol [25, 41].

The investigated strain conditions mimic the strain path for many cardiovascular medical implants and are therefore relevant to the material fatigue characterization of VAR/EBR Nitinol for Class III medical device applications. The FSL line shows the experimental boundary between survival/fracture that simulate in vivo conditions, whereby below this FSL line there is a greater probability of survival to $\geq 10^8$ and above the line there is a greater probability of fracture $\leq 10^8$ cycles. No further statistical analyses were conducted with these data, as are routinely done to calculate medical device fatigue safety factors [2, 45].

Figure 6 also demonstrates that the VAR/EBR 10^8-cycle FSL data are substantially greater than the 10^7-cycle FSL for VAR Nitinol [25, 41] (black line) at each mean strain. Specifically, at mean strains between 3 and 5%, VAR/EBR Nitinol provides an 275% increase in FSL compared with VAR Nitinol. The results from VAR/EBR Nitinol demonstrate the critical impact of limiting the inclusion size (longitudinal orientation) to < 10 µm in the final product compared with the ~ 100 µm inclusion length for the VAR [32], or ~ 40 µm length for VAR II or VIM/VAR II Nitinol [32–34]. In a separate manuscript (Pelton et al. in preparation 2025), comparable diamond test coupons were manufactured from Nitinol tubing with a range of microstructural purity that were subjected to comparable thermomechanical processing (and therefore similar microstructures except inclusions). The main factor to differentiate these test

Table 3 10^8 cycles bending fatigue results of VAR/EBR Nitinol tested at 9% pre-strain and variable mean strain and strain amplitudes in 37 °C distilled water

Mean strain (%)	Strain amplitude (%)	Number of component lots tested	Sample size	Total fractured specimens	Survival probability (%)
0.50	0.75	3	6	0	100
0.50	1.00	2	6	1	83
1.00	1.00	3	6	0	100
1.00	1.50	2	6	0	100
1.00	1.25	2	6	0	100
1.00	1.75	3	6	6	0
1.50	1.35	1	6	0	100
1.50	1.50	3	9	0	100
1.50	1.75	3	6	2	67
1.50	2.00	1	6	6	0
3.00	2.00	3	9	0	100
3.00	2.25	1	6	0	100
3.00	2.50	1	6	2	67
5.00	2.00	3	9	0	100
5.00	2.25	1	6	0	100
5.00	2.50	2	3	2	33
7.00	1.25	3	6	0	100
7.00	1.50	4	9	2	78
7.00	1.75	1	6	6	0
Total			123	27	

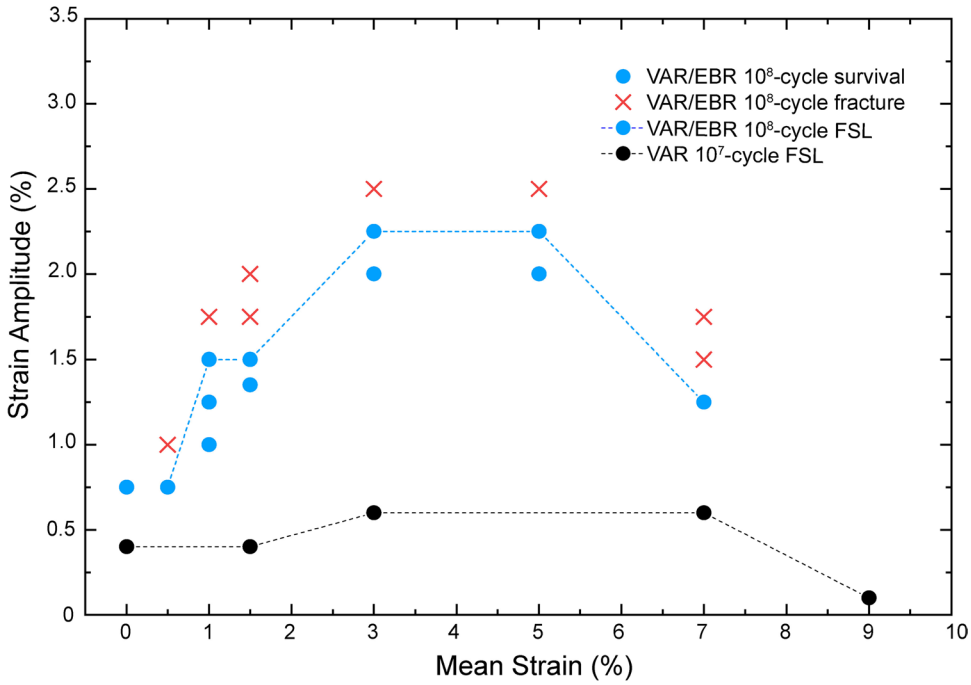

Fig. 6 10^8-Cycle Fatigue Strain Limit (FSL) diagram of VAR/EBR Nitinol under cyclic bending conditions. Here the fatigue data are plotted as a function of mean strain (abscissa) and strain amplitude (ordinate). The blue circles are conditions that survived the 10^8 cycles, whereas the X symbols indicate conditions that resulted in at least one fracture prior to 10^8 cycles. The blue line is a visual indicator of the resultant 10^8-cycle FSL. By way of comparison, the black line illustrates previous published 10^7-cycle FSL diagram from VAR Nitinol under cyclic bending conditions [25, 41]

coupons was the size and distribution of the NMIs. As such, the current results are consistent with the mounting evidence that reduction of NMI size and distribution is a primary factor that results in improved fatigue results.

Figure 7 shows typical fracture surfaces from representative (a) VAR/EBR and (b) VAR Nitinol. The circles on both images indicate the initiation locations for the fatigue fractures. The initiation site on both samples was on the diamond strut extrados that undergoes cyclic tensile strains, in accord with FEA predictions. The VAR specimen was processed from 7 × 0.5 mm tubing with comparable mechanical and thermal properties as the VAR/EBR shown in Fig. 6. The VAR specimens were subjected to a 9% pre-strain, unloaded to 3% mean strain (unloading plateau) and cycled with 0.4% strain amplitude. These more recent fatigue results were comparable to those from the earlier studies [25, 41]. From this SEM image, it is clear that fracture initiated at an oxide inclusion (and associated void; i.e., the so-called particle-void assembly [46]); fracture occurred at 30,000 cycles according to the continuous force–displacement data. The

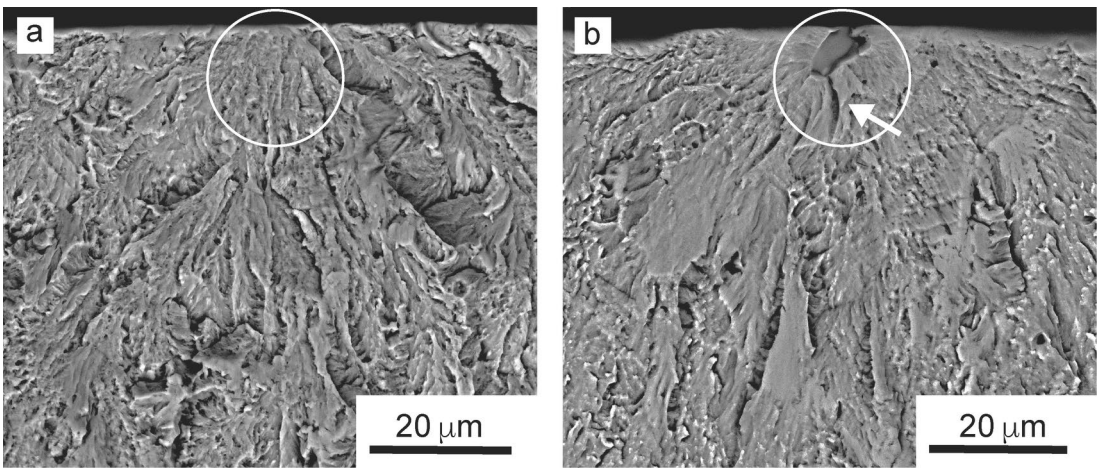

Fig. 7 **a** SEM (backscattered image) fracture surface from VAR/EBR Nitinol under conditions of 3% mean strain and 2.5% strain amplitude that fractured at 91,000,000 cycles. The fracture initiation location is marked with a circle. No inclusions were observed near the initiation site. **b** SEM (backscattered image) fracture surface from a VAR Nitinol under conditions of 3% mean strain and 0.4% strain amplitude, where fracture occurred at 30,000 cycles. The fatigue crack initiation is at the circled location where there is a ~ 9μm (transverse) non-metallic inclusion as well as an accompanying crack (arrowed)

arrow indicates a secondary crack that appears to emanate from the oxide inclusion, which is typical in Nitinol fatigue fractures that contain oxide and carbide inclusions. In contrast, there is no evidence of an inclusion at the initiation site for the VAR/EBR Nitinol (9% pre-strain, unload to 3% mean strain with 2.5% strain amplitude) that fractured at 91,000,000 cycles.

Similar to previously reported bending fatigue data using a similar coupon geometry and test method [25, 41], the FSL behavior can be described in three distinct strain regimes: (i) a strong dependence of the mean strain with increase in the FSL with mean strains up to 3%, (ii) non-sensitivity to mean strains between 3 and 5%, and (iii) a decrease in FSL beyond 5%. The data indicate that the fatigue resistance of the material is bounded by regions with lower FSL where cyclic martensitic phase transformation initiates (0.5 to 3.0% mean strain) and beyond ~ 5% where the stress-induced martensitic transformation saturates. In contrast, the fatigue life remains relatively independent of mean strain within the plateau region.

Discussion

The material fatigue characterization of VAR/EBR Nitinol material is represented with a conventional FSL diagram as exemplary in Fig. 6 that provides the 10^8-cycle constant life of test coupons under simulated medical device in vivo conditions. Specifically, a combination of conditions that spans multiple mean strain and strain amplitudes was tested and analyzed. Such constructions are used to define the likelihood of fracture and survival and are often employed as a prediction tool to define the safety factor of a device subjected to in vivo loading conditions.

The strain values presented in Fig. 6 are calculated with a state-of-the-art commercial structural simulation code as discussed in Sect. "Materials and Methods". For more complex geometries and loading conditions, the assessment of local strains from global displacements, especially with superelastic Nitinol, has inherent sources of variabilities. The FEA "goodness of fit" between, for example, the force–displacement of the test article and the simulation depends on the quality of the input parameters (uniaxial tensile data) as well as the uniformity of the individual coupon mechanical properties and dimensional variations. As demonstrated in Fig. 3 the tensile behavior has very little variability within each tube manufacturing lot and between the two lots up to the crimp strain of 9%; the DSC results are also consistent. Furthermore, the UMAT values summarized in Table 2 show that the input FEA parameters are comparable; side-by-side comparison indicate that the resultant FEA strain values are well within 6% of each other for the two tubing manufacturing lots. Consequently, for the purpose of this paper, the fatigue results are pooled.

Each of the 19 fatigue conditions presented in this investigation was subjected to FEA validation procedures for both the crimp cycle as well as the cyclic conditions. One such example is shown for diamonds that were crimped to 9% tensile strain and unloaded to the mean strain of 1.5% (Fig. 2c) and then cycled with a strain amplitude of 1.5% (Fig. 2d). The FEA crimp cycle estimation encompasses the scatter in the benchtop data quite well. In addition, the FEA model for the cyclic motion is also well aligned with the force–displacement data where the simulation covers the majority of the cyclic data. In general, for these correlations between bending motion and computational simulation, slight dimensional variations (especially strut width) can lead to these offsets. For medical device testing and analysis, it is recommended to conduct a full sensitivity analysis, including an analysis of the force–displacement simulation at nominal as well as maximum and minimum dimensions [37], which is beyond the scope of the present investigation.

Furthermore, the predicted strains for a complex medical device design are represented as "point clouds" where each FEA element represents the stress/strain state of a location in a device that often extends multiple mean strains and strain amplitudes (see, for example [47]). The fatigue strain condition of a test coupon (i.e., diamond-, Z- or C-shaped specimen) is often represented as a single data point [25, 27, 48] that corresponds to what is defined as the maximum mean strain and maximum strain amplitude location for this specific strain condition. The element with the maximum mean strain and maximum strain amplitude match when model convergence is established. These conditions traditionally predict the worst-case strain condition that yields survival or fracture. Post-mortem visual inspections can be performed to confirm the fracture location and the validity of the FEA model prediction. However, this approach can be simplistic for certain combinations of mean strain and strain conditions in superelastic Nitinol. For conditions of high mean strain (e.g., beyond the stress plateau) and high strain amplitudes, the FEA fatigue strain point cloud of the test specimens shows divergence, where the maximum mean strain location does not match the location of the maximum strain amplitude. As the mean strain increases further beyond the stress plateau, the divergence behavior becomes more severe and appears at even lower strain amplitudes. Figure 8 provides the point cloud for the nominal strain conditions that define the FSL line in Fig. 6; for simplicity, only the survival conditions are shown. For example, the nominal $7 \pm 1.25\%$ condition yields a maximum predicted strain amplitude of 1.25% at 5.04% mean strain at one location, and a strain amplitude of 0.73% at 7.00% mean strain at another location. As such, representation of $7 \pm 1.25\%$ with a single point might be misleading, while in fact the point

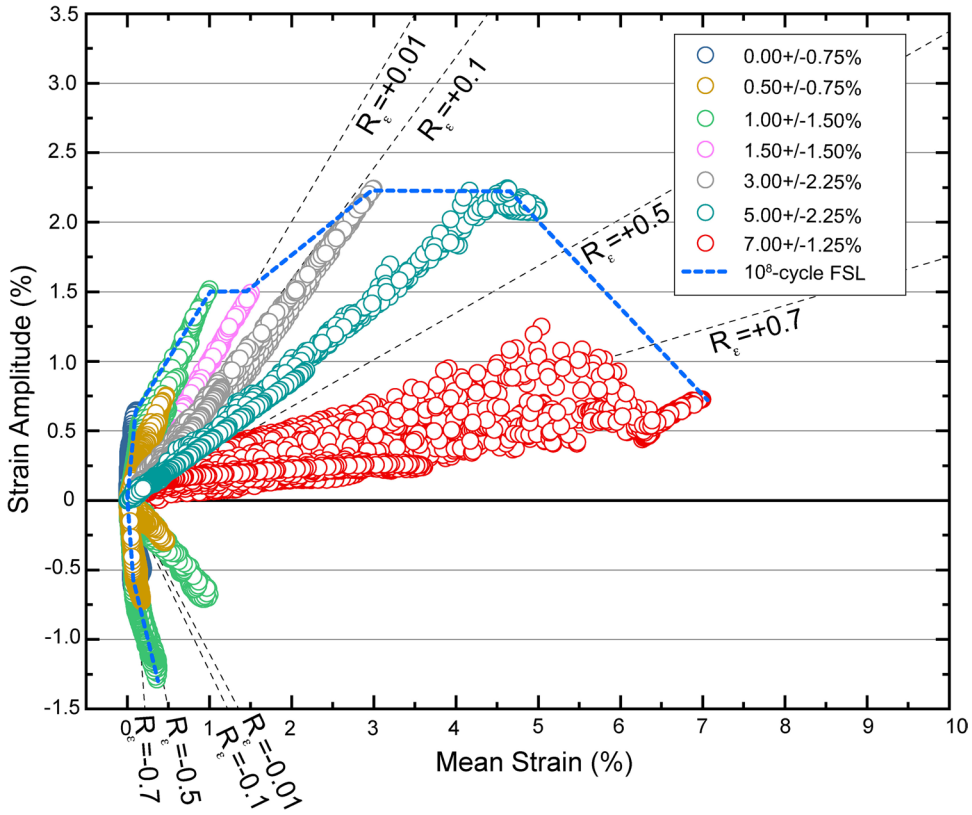

Fig. 8 FEA "point clouds" of the 10^8 cycles run out strain conditions. The 10^8 Fatigue Strain Limit (FSL) line that contours the "point clouds" is provided as a dotted blue line. The 0.00 ± 0.75% and 7.00 ± 1.25% strain condition demonstrate divergence of the "point cloud"

cloud represents a more realistic reporting of the entire strain conditions in the diamond coupon. Conversely, for conditions of low mean strain and high strain amplitudes, where the strain amplitude exceeds the mean strain, the tension and compression sides of an apex under bending condition revert during cyclic loading. These situations make the prediction for fracture more difficult (e.g., initiation at intrados *vs* extrados). Both cases are limitations to represent a nominal strain condition (mean plus amplitude) as a single data point on a Nitinol FSL diagram. Furthermore, the nominal conditions of 0.00 ± 0.75%, 0.50 ± 0.75%, 1.00 ± 1.50%, and 1.50 ± 1.50% provide a complex stress/strain state during cyclic loading.

In the presented models, both mean strain and strain amplitude were determined using a tensor method. This approach first calculated the strain across all six tensor components (three axial and three shear), and then reported the maximum principal vector of these components. To obtain the strain amplitude tensors, the strains are subtracted between the different deformation states; specifically, comparing loaded and unloaded conditions of the test specimen. When calculating strain amplitude tensors, the strain tensors are obtained by subtracting the two deformation states (loaded *vs.* unloaded) of the test specimen. The calculation process is straightforward when elements remain consistently in tension or compression across both deformation states. However, complications arise when elements transition between tension and compression. In such cases, the delta strain tensors can be calculated in two ways: either by subtracting the unloaded state from the loaded state, or vice versa. Thus, for specific strain conditions (0.00 ± 0.75%, 0.50 ± 0.75%, and 1.00 ± 1.50%), where the strain amplitudes exceed the mean strain, the calculation was performed in both directions and the resulting strain amplitude clouds are shown above (positive) and below (negative) of the mean strain axis (Fig. 8). This visualization offers detailed insights into the reverting loading mode of elements under near-zero mean strain conditions, where the strain ratio R_ε ($= \varepsilon_{min}/\varepsilon_{max}$) approaches − 1. The effect of strain ratio, R_ε ($= \varepsilon_{min}/\varepsilon_{max}$), is also considered for $-1 < R_\varepsilon < 1$ (Fig. 8). The fatigue strain limit of the VAR/EBR appears to be optimal for $0.1 < R_\varepsilon < 0.5$.

Previously reported data on tension-tension testing of VAR Nitinol wire [10] and VIM/VAR Nitinol sheet [24], respectively, indicate that the 10^7-cycle fatigue threshold under pure Mode I-type loading is the strain amplitude that separates linear austenite (plus approximately constant martensite) cyclic loading and SIMT loading. Both studies concluded that the upper plateau stress represents the maximum stress for survival during fatigue cycling within a two-phase austenite/martensite region. Loading that involves cyclic stress-induced martensitic transformation, i.e., when the cyclic stress exceeds the fatigue threshold (defined as a stress hysteresis) resulted in fatigue

failures at less than 10^7 cycles. In contrast, loading without continuous SIMT, where deformation is nominally "elastic" (with a minor anelastic component and perhaps some austenite to R-phase transformation), led to runouts up to 10^7 cycles in a majority of the samples. The fatigue threshold defined as the strain amplitude limit that separates the two regimes is determined by the forward and reverse transformation stresses or plateau stresses and the effective cyclic modulus. Once the stress amplitude exceeds the stress hysteresis, the slope decreases due to increased martensite volume fraction and defect generation. As such there is growing evidence that even under displacement- or strain-controlled cyclic testing, the maximum local stresses play an important role in Nitinol fatigue behavior. See, for example, Nitinol rotary bend fatigue ($R_\varepsilon = -1$) test results whereby there is an approximate constant fatigue life within the stress plateau region of superelastic $Ni_{50.8}Ti_{49.2}$ wires [49, 50].

However, and as noted by Launey, et al. [10] and Catoor, et al. [24], if the fatigue limit depends only on monotonic behavior, the role of inclusions in fatigue requires clarification. The loading mode in the current work is different from previous investigations [10, 24], i.e., mixed Mode I/II (bending) vs pure Mode I (tension) loading. Nevertheless, the fatigue strain amplitude that results in 10^8-cycle run out conditions extend far beyond into the cyclic SIMT region with a concomitant significant stress hysteresis [39]. The 10^8- cycle FSL within the two-phase austenite/martensite region, i.e., 3 and 5% mean strain, is reported at 2.25% that represent a remarkable cyclic strain range of 4.5% that dissipates a large amount of transformational energy. It is given that inclusions are observed at crack initiation sites [10, 28, 29, 32, 48, 51] in the majority of Nitinol fatigue investigations. These observations imply that the fatigue limit of Nitinol is dictated by the stress intensity threshold, ΔK_{th}, required for crack initiation from these inclusions. As such, the larger the inclusion, the smaller stress amplitude is required to grow the crack. Cyclic stress-induced martensitic transformation plays a dominant role in the fatigue behavior of superelastic Nitinol. It is hypothesized that for inclusions of the size encountered in the present study (i.e., ≤ 10 μm), inclusions are merely proximate causes of fatigue crack initiation, while the SIMT serves as the primary one. Conversely, if the inclusions and/or defects (e.g., voids) exceed a certain dimension, the crack initiation threshold from inclusions may become lower than the SIMT fatigue limit. Thus, depending on the inclusion size (nominal diameter and length), either the SIMT or the inclusions could determine the fatigue crack initiation threshold. Furthermore, the fatigue limit within the two-phase region is limited by the SIMT threshold, and therefore cannot be increased indefinitely by reducing the inclusion size. The authors here speculate that a critical inclusion size may exist under which the fatigue limit of the material is solely driven by the stress–strain response of the material [52, 53].

Many of the superelastic Nitinol fatigue investigations have focused on several key fracture mechanics parameters associated with the onset of subcritical and critical cracking of so-called large cracks [52, 54–59]. These studies provided insight on possible initiation sites (e.g., inclusions), effects of crystallography (i.e., drawing and rolling directions) as well as ΔK_{th}, values that could be used for device design and safety efficacy. However, this is a rather arbitrary assignment of the threshold for cardiovascular devices. For physiological frequencies (e.g., due to the cardiac cycle), these conditions translate to crack extensions of a few millimeters per year. This crack growth range is somewhat precarious when dealing with small devices such as stents that may contain physically small flaws. Unlike the relatively large cracks found in laboratory fatigue specimens, typically millimeters in length, biomedical devices are likely to contain far smaller flaws on the order of tens of micrometers in size, e.g., microstructural voids, inclusions and/or crack-like defects. Thresholds for such small cracks tend to be lower than the large-crack thresholds, referred to as the "small-crack effect" [60–63].

A recent body of work has begun to investigate the possible effects of small cracks in superelastic Nitinol. Robertson and Ritchie [52] suggested a linear extrapolation of the crack-growth data on a log–log fatigue-crack growth-rate, da/dN, curve in order to determine the approximate stress intensity threshold for small crack, $\Delta K_{th,\,small\,crack}$ [64]. These authors speculated that whereas the large-crack behavior is due to crack closure from multiple effects (e.g., interference or wedging of oxidation debris or fracture surface asperities inside the crack flanks), small cracks are not subjected to these same closure effects. Consequently, $\Delta K_{th,\,small\,crack}$ is thought to be some 40–60% lower than for large cracks based on this extrapolation [16, 52]. Recent publications expounded on the differences of small cracks *vs* large cracks. Specifically, Malito, et al. investigated superelastic Nitinol wires in tension-tension with focused-ion beam starter cracks to a 10^7-cycle run out [53]. Their hybrid S–N and fracture mechanics-based fatigue approach provided data to differentiate between conditions where the defect area is small enough that cracks are not expected to grow. Under these conditions of small cracks, a total-life fatigue approach may be more appropriate. Malito et al. measured a $\Delta K_{th,\,small\,crack}$ of 0.34 MPa$\sqrt{m}$ under uniaxial tension at a pre-strain of 6%, mean strain of 3%, and R = 0.75. As the defect area increased in size, there was a decrease in the allowable stress amplitude for run out. This approach follows the original construction by Kitagawa and Takahashi [65] and allows quantification of the critical defect size. For a crack length smaller than a critical crack size, the stress range (or stress amplitude) departs gradually from $\Delta K_{th.}$

Furthermore, as the crack length decreases, the threshold stress range approaches asymptotic to a constant stress range level, which is approximately equal to the fatigue limit of the unnotched smooth (flaw- or defect-free) specimen of the material. Malito, et al. indicated that the critical small crack length for Mode I cycling is on the order of 10 µm, whereby defect sizes greater than this value can tolerate lower stress amplitudes. This value correlates well with the work from Robertson and Ritchie [52].

As mentioned above, the maximum inclusion size for the VAR/EBR material is less than the critical small crack length of 10 µm. In this regime, the fatigue life of a VAR/EBR Nitinol product is dictated by its duty cycle stresses/strains and is therefore insensitive to the flaw size such as defects, cracks, inclusions and/or voids. The device life cycle can tolerate lower duty cyclic stresses/strains as the flaw size increases to values greater than the critical small crack length of ~ 10 µm. This results in a lower fatigue limit of the product. As such, the development of VAR/EBR material with inclusion sizes less than the critical small crack length represents a paradigm shift in the design of life-supporting medical devices. An upcoming paper by Pelton, et al. will provide a statistical analysis of both transverse and longitudinal inclusion length for six varieties of superelastic Nitinol, whereby the measured $K_{\text{th,small crack}}$ under bending conditions is < 10 µm in the final material size. The corresponding fatigue results from these materials are consistent with this concept of a critical small crack size under bending fatigue conditions.

The inclusion size and distribution clearly affect the fatigue behavior of Nitinol as documented in the above discussions. In addition, thermomechanical processing also influences the fatigue properties as demonstrated in previous investigations. The present (S)TEM microstructural investigation of the VAR/EBR diamond test specimens reveals that the thermal treatments of the tubing and device produced a partially recrystallized microstructure with ~ 150 nm longitudinal grain size [39]. These fine-grain structures appear to be stable against the conditions of 9% pre-strain, as well as 9% pre-strain with unload to 3% mean strain and 2% strain amplitude to 10^8 cycles. Unlike fatigue structures with larger grain sizes, there does not seem to be an increase in dislocation density during cycling. A forthcoming manuscript in preparation by these current authors will focus on (S)TEM microdiffraction results, grain orientations, and the effects of stress–strain hysteresis as well as a comparison between the microstructures from the tension and compression regions of the test coupons. These results align well with previous investigations of processing effects on medical-grade superelastic Nitinol fatigue. For example, Pelton [41] compared tension-tension fatigue cycling (1.5% mean strain and 0.25% strain amplitude) and TEM of ø3mm VAR Nitinol ($Ni_{50.8}Ti_{49.2}$) rods under conditions of full anneal (900°C for 30 min) and superelastic anneal (510°C for 10 min). The fully annealed Nitinol (with an initial transverse grain size of ~ 50 µm) showed a decrease in hysteresis width, an increase in cyclic modulus, with cyclic hardening (illustrated with a decrease in the unloading plateau stress) within 100 fatigue cycles. The TEM microstructure in the transverse orientation after only 10 cycles consisted of banded austenite and deformed martensite with a high density of dislocations (~ 10^{14} m^{-2}) with < 100 > {011} slip systems in the B2 austenite, similar to the microstructures observed in thermally cycled Nitinol [15, 66, 67] and mechanically fatigued Nitinol [68]. In contrast, the fatigued specimens with the superelastic anneal condition demonstrated a more stable stress hysteresis with minimal work hardening and more constant cyclic modulus. Furthermore, the microstructure of these specimens consisted of ~ 75 nm transverse grain size with significantly lower dislocation density and no apparent retained martensite, similar to the non-fatigued microstructures. Delville, et al. conducted an interesting and informative investigation on the effects of processing and uniaxial fatigue cycling on the microstructure evolution $Ni_{50.8}Ti_{49.2}$ wires [42]. In their study, the as-drawn wires were electrically pulsed between 4 and 18 ms to simulate thermal treatments. These heat-treated wires were then mechanically strained up to 8% or 1500 MPa for ten cycles. The resultant microstructures were characterized with TEM post-tensile testing and correlated to the stress–strain curves. The optimal cyclic properties were observed with for these 100 µm diameter wires with partially polygonized and recrystallized transverse microstructures that consisted of 20 to 50 nm nanograins. Electrical pulse treatments that resulted in grain growth showed evidence of dislocation formation and permanent set in the stress–strain curves as a result of the low-cycle fatigue cycling.

The landscape for design and fatigue durability of medical devices is greatly enhanced with the greater FSL afforded by VAR/EBR Nitinol primarily due to the smaller inclusion sizes, lower area fraction, as well as optimal thermomechanical processing. As an illustration on how VAR/EBR Nitinol can enhance the design and safety of medical devices across multiple mean strains, one can evaluate the designs of many novel heart valve replacement frames. These modern designs (e.g., aortic, mitral, and tricuspid) may incorporate two or more sections of the device in order to provide optimized mechanical performance in vivo. The “inner device” is attached to the tissue (or polymeric) valve and flexes with the opening and closing of the valve during the pulse pressures associated with the cardiac cycle. Therefore, this inner section of the heart valve frame is generally designed to be stiffer than the “outer device” with little or no oversizing. Consequently, the mean strains of the inner device are typically lower (e.g., ≤ 1.5%) and, therefore, the strain amplitudes could be greater or equal to the mean strains

during in vivo use. In contrast, the purpose of the connected outer device is to conform to the anatomy of the heart valve chamber with effective device diameters greater than the anatomy to provide an interference fit to aid in positioning and anchoring. Consequently, the mean strains of the outer device are generally observed to be ≥ 1.5% and could extend to be ≥ 6%. For peripheral and neurovascular cardiovascular devices, there could be a range of oversize conditions that result in mean strains from 0 to 8%. The in vivo strain amplitudes for these Nitinol-based cardiovascular devices have traditionally been limited to ~ 0.5% due to the corresponding FSL of Nitinol with larger inclusions. As such, the 10^8-cycle FSL of VAR/EBR Nitinol represents a significant enhancement of the safety operation of complex devices operating across multiple mean strains with extended allowable strain amplitudes.

Conclusion

This investigation demonstrates that VAR/EBR Nitinol with inclusion sizes below 10 µm (measured in the hot-worked EBR state) exhibits unprecedented fatigue performance that achieves improvement up to 275% in its 10^8-cycle Fatigue Strain Limit compared to conventional VAR Nitinol under clinically relevant strain conditions. The VAR/EBR fatigue behavior across multiple mean strains (0–7%) reveals characteristic regimes that correlate with phase transformation mechanisms, with optimal performance in the 3–5% plateau region. The enhanced fatigue resistance is primarily attributed to the ultra-clean microstructure with significantly reduced inclusion size and area fraction as well as optimal microstructures.

These findings suggest that when inclusion sizes are below a critical small crack length of approximately 10 µm, fatigue performance becomes predominantly dictated by cyclic stress/strain response rather than flaw size. This represents a fundamental advancement in understanding Nitinol fatigue mechanisms and enables a paradigm shift in cardiovascular device design methodology. Improvements in the thermomechanical processing to stabilize the microstructure (e.g., to produce ≤ 150 nm sized grains) also plays a significant role in the improved fatigue behavior of Nitinol.

The exceptional fatigue properties of VAR/EBR Nitinol substantially expand design possibilities for complex cardiovascular devices that operate across varied mechanical environments, particularly for critical applications like heart valve frames that experience different strain regimes within a single device. These observations provide designers with significantly enhanced safety margins for life-supporting and life-sustaining implantable devices, potentially extending service life beyond current regulatory requirements.

Acknowledgements Part of this work was performed at Stanford Nano Shared Facilities and we acknowledge the use of the equipment and assistance from SNSF staff. We acknowledge the assistance from L. Dertinger of ADMEDES GmbH as well as from N. D'Attilio, P. Hempel, and R. Hoffmann of G.RAU Inc. The authors also acknowledge the financial support for this investigation from Euroflex GmbH.

References

1. Duerig T, Pelton A, Stoeckel D (1999) An overview of Nitinol medical applications. Mater Sci Eng A 273–275:149–160
2. ISO5840-1 (2021) Cardiovascular implants—cardiac valve prostheses Part 1: general requirements
3. FDA (2021) Technical considerations for non-clinical assessment of medical devices containing nitinol
4. ASTM (2018) F2063 standard specification for wrought nickel-titanium shape memory alloys for medical devices and surgical implants,
5. ASTM (2023) F2082 standard test method for determination of transformation temperature of nickel-titanium shape memory alloys by bend and free recovery
6. ASTM (2019) F2942 standard guide for in vitro axial, bending, and torsional durability testing of vascular stents
7. ASTM (2022) F2516 standard test method for tension testing of nickel-titanium superelastic materials
8. Aguel F, Hillebrenner M, Stewart SFC, Swain J, Hampshire V, Zuckerman B (2011) U.S. regulatory considerations for heart valves implanted by minimally invasive surgery. Cardiovasc Eng Technol 2(2):62–65
9. Pelton AR, Berg BT, Saffari P, Stebner AP, Bucsek AN (2022) Pre-strain and mean strain effects on the fatigue behavior of superelastic Nitinol medical devices. Shape Mem Superelasticity 8(2):64–84
10. Launey ME, Ong I, Berg BT, Pelton AR (2023) Considerations on tension-tension fatigue predictions for Nitinol. Shape Mem Superelast 9(1):97–115
11. Pelton AR, Clausen B, Stebner AP (2015) In situ neutron diffraction studies of increasing tension strains of superelastic nitinol. Shape Mem Superelast 1(3):375–386
12. Stebner AP, Paranjape HM, Clausen B, Brinson LC, Pelton AR (2015) In-situ neutron diffraction studies of large monotonic deformations of superelastic Nitinol. Shape Mem Superelasticity 1:252–267
13. ASTM (2017) E3098–17 standard test method for mechanical uniaxial pre-strain and thermal free recovery of shape memory alloys. ASTM International
14. Sehitoglu H, Alkan S (2018) Recent progress on modeling slip deformation in shape memory alloys. Shape Mem Superelasticity 4:11–25

15. Mohammed ASK, Sehitoglu H (2020) Martensitic twin boundary migration as a source of irreversible slip in shape memory alloys. Acta Mater 186:50–67
16. Robertson SW, Pelton AR, Ritchie RO (2012) Mechanical fatigue and fracture of Nitinol. Int Mater Rev 57(1):1–36
17. Tabanli RM, Simha NK, Berg BT (1999) Mean stress effects on fatigue of NiTi. Mater Sci Eng A A 273–275:644–648
18. Tabanli RM, Simha NK, Berg BT (2001) Mean strain effects on the fatigue properties of superelastic NiTi. Metall Mater Trans A Phys Metall Mater Sci 32A(7):1866–1869
19. Tolomeo D, Davidson S, Santinoranout M (2000) Cyclic properties of superelastic nitinol: design implications. In: Russell SM, Pelton AR (eds) SMST-2000—proceedings of the international conference on shape memory and superelastic technologies. Internationa Organization on SMST, Pacific Grove, pp 409–417
20. Morgan NB, Painter J, Moffat A (2003) Mean strain effects and microstructural observations during in vitro fatigue testing of NiTi. In: Pelton AR, Duerig TW (eds) SMST-2003: proceedings of the international conference on shape memory and superelastic technologies. International Organization on SMST, Pacific Grove, pp 303–310
21. Shaw JA, Kyriakides S (1997) On the nucleation and propagation of phase transformation fronts in a NiTi alloy. Acta Mater 45(2):683–700
22. Barney MM, Xu D, Robertson SW, Schroeder V, Ritchie RO, Pelton AR, Mehta A (2011) Impact of thermomechanical texture on the superelastic response of Nitinol implants. J Mech Behav Biomed Mater 4(7):1431–1439
23. Reedlunn B, Churchill CB, Nelson EE, Shaw JA, Daly SH (2014) Tension, compression, and bending of superelastic shape memory alloy tubes. J Mech Phys Solids 63:506–537
24. Catoor D, Ma Z, Kumar S (2019) Cyclic response and fatigue failure of Nitinol under tension–tension loading. J Mater Res 34:3504–3522
25. Pelton AR, Schroeder V, Mitchell MR, Gong X-Y, Barney M, Robertson SW (2008) Fatigue and durability of Nitinol stents. J Mech Behav Biomed Mater 1:153–164
26. Gopal S, Kim S, Swift R, Choules B (2008) Fatigue life estimation of nitinol medical devices. 2008 Abaqus Users' conference
27. Cao H, Wu MH, Zhou F, McMeeking RM, Ritchie RO (2020) The influence of mean strain on the high-cycle fatigue of Nitinol with application to medical devices. J Mech Phys Solids. https://doi.org/10.1016/j.jmps.2020.104057
28. Weaver JD, Sena GM, Aycock KI, Roiko A, Falk WM, Sivan S, Berg BT (2023) Rotary bend fatigue of Nitinol to one billion cycles. Shape Mem Superelasticity 9(1):50–73
29. Roiko A, Cook S, Berg B, Falk W, Weaver JD (2025) Observation and modeling of potential sub-threshold damage growth mechanism for nitinol in ultra-high cycle fatigue. Int J Fatigue. https://doi.org/10.1016/j.ijfatigue.2024.108613
30. Moumni Z, Herpen AV, Riberty P (2005) Fatigue analysis of shape memory alloys: energy approach. Smart Mater Struct 14(5):S287–S292
31. Mahtabi MJ, Shamsaei N (2016) A modified energy-based approach for fatigue life prediction of superelastic NiTi in presence of tensile mean strain and stress. Int J Mech Sci 117:321–333
32. Robertson SW, Launey M, Shelley O, Ong I, Vien L, Senthilnathan K, Saffari P, Schlegel S, Pelton AR (2015) A statistical approach to understand the role of inclusions on the fatigue resistance of superelastic Nitinol wire and tubing. J Mech Behav Biomed Mater 51:119–131
33. Pelton AR, Pelton SM, Jörn T, Ulmer J, Niedermaier D, Plaskonka K, LePage WS, Saffari P, Mitchell MR (2019) The quest for fatigue-resistant nitinol for medical implants. In: Mitchell MR, Berg BT, Woods TO, Jerina KL (eds) STP1616: fourth symposium on fatigue and fracture of metallic medical materials and devices. ASTM International, West Conshohocken, pp 1–30
34. Pelton AR, Pelton SM, Ulmer J, Niedermaier D, Plaskonka K, Mitchell MR, Saffari P (2017) The use of next generation Nitinol for medical implants. In: Chakfé N, Heim F, Meichelboeck W (eds) European symposium on vascular biomaterials. Geprovas, Strasbourg, pp 35–44
35. Choudhury A, Hengsberger E (1992) Electron beam melting and refining of metals and alloys. ISIJ Int 32(5):673–681
36. ASTM (2018) F2516 standard test method for tension testing of nickel-titanium superelastic materials
37. ASTM (2021) F2514 finite element analysis (FEA) of metallic vascular stents subjected to uniform radial loading
38. FDA (2016) Reporting of computational modeling studies in medical device submissions
39. Pelton AR, Pelton SM, Launey ME, Nagaraja S, Keck A, Plaskonka-Weisenburger K, Knoll S, Ulmer J, Saffari P, Czaja P, Barnum A, Sinclair R (2024) Development of high-durability nitinol for heart valve frames, SMST 2024. ASM International, Cascais, Portugal
40. Delville R, Malard B, Pilch J, Sittner P, Schryvers D (2010) Microstructure changes during non-conventional heat treatment of thin Ni–Ti wires by pulsed electric current studied by transmission electron microscopy. Acta Mater 58(13):4503–4515
41. Pelton AR (2011) Nitinol fatigue: a review of microstructures and mechanisms. J Mater Eng Perform 20(4):613–617
42. Delville R, Malard B, Pilch J, Sittner P, Schryvers D (2011) Transmission electron microscopy investigation of dislocation slip during superelastic cycling of Ni–Ti wires. Int J Plast 27(2):282–297
43. Tyc O, Molnárová O, Šittner P (2021) Effect of microstructure on fatigue of superelastic NiTi wires. Int J Fatigue 152:106400
44. Ophus C (2019) Four-dimensional scanning transmission electron microscopy (4D-STEM): from scanning nanodiffraction to ptychography and beyond. Microsc Microanal 25(3):563–582
45. ASTM (2017) F3211−17 standard guide for fatigue-to-fracture (FtF) methodology for cardiovascular medical devices
46. Rahim M, Frenzel J, Frotscher M, Pfetzing-Micklich J, Steegmüller R, Wohlschlögel M, Mughrabi H, Eggeler G (2013) Impurity levels and fatigue lives of pseudoelastic NiTi shape memory alloys. Acta Mater 61(10):3667–3686
47. Marrey R, Baillargeon B, Dreher ML, Weaver JD, Nagaraja S, Rebelo N, Gong X-Y (2018) Validating fatigue safety factor calculation methods for cardiovascular stents. J Biomech Eng 140(6):061001–061001-9
48. Launey M, Robertson SW, Vien L, Senthilnathan K, Chintapalli P, Pelton AR (2014) Influence of microstructural purity on the bending fatigue behavior of VAR-melted superelastic Nitinol. J Behav Biomed Mater 34:181–186
49. Kim Y, Miyazaki S (1997) Fatigue life of Ti-50 at.% Ni and Ti-40Ni-10Cu (at.%) shape memory alloy wires. In: Pelton AR, Russell S, Hodgson D, Duerig TW (eds) Shape memory and superelastic technologies-97. SMST, Asilomar, pp 473–478
50. Pelton AR, Fino-Decker J, Vien L, Bonsignore C, Saffari P, Launey M, Mitchell MR (2013) Rotary-bending fatigue characteristics of medical-grade Nitinol wire. J Mech Behav Biomed Mater 27:19–32
51. Urbano MF, Cadelli A, Sczerzenie F, Luccarelli P, Beretta S, Coda A (2015) Inclusions size-based fatigue life prediction model of *NiTi* alloy for biomedical applications. Shape Mem Superelast 1(2):240–251
52. Robertson SW, Ritchie RO (2008) A fracture-mechanics-based approach to fracture control in biomedical devices manufactured from superelastic Nitinol tube. J Biomed Mater Res B Appl Biomater 84B:26–33

53. Malito LG, Haghgouyan B, Bowers ML, Rosen A, Amin-Ahmadi B, Robertson SW, Ritchie RO (2024) Fatigue and fracture of small cracks in superelastic nitinol. Int J Fatigue. https://doi.org/10.1016/j.ijfatigue.2024.108208
54. Dauskardt RH, Duerig TW, Ritchie RO (1989) Effects of in situ phase transformation on fatigue-crack propagation in titanium–nickel shape-memory alloys. In: Proceedings of the MRS international meeting on advanced materials, Vol. 9: shape memory materials; Tokyo, 31 May–3 June 1988 (1989), pp 243–249
55. McKelvey AL, Ritchie RO (1999) Fatigue-crack propagation in Nitinol, a shape-memory and superelastic endovascular stent material. J Biomed Mater Res A 47(3):301–308
56. Holtz RL, Sadananda K, Imam MA (1999) Fatigue Thresholds of Ni-Ti alloy near the shape memory transition temperature. Int J Fatigue 21:S137–S145
57. McKelvey AL, Ritchie RO (2001) Fatigue-crack growth behavior in the superelastic and shape-memory alloy Nitinol. Metall Mater Trans A (Phys Metall Mater Sci) 32A(3A):731–743
58. Stankiewicz JM, Robertson SW, Ritchie RO (2007) Fatigue-crack growth properties of thin-walled superelastic austenitic Nitinol tube for endovascular stents. J Biomed Mater Res A 81A(3):685–691
59. Robertson SW, Mehta A, Pelton AR, Ritchie RO (2007) Evolution of crack-tip transformation zones in superelastic Nitinol subjected to in situ fatigue: a fracture mechanics and synchrotron X-ray microdiffraction analysis. Acta Mater 55(18):6198–6207
60. Suresh S, Ritchie RO (1984) Propagation of short fatigue cracks. Int Met Rev 29(6):445–475
61. Ritchie RO, Lubock P (1986) Fatigue life estimation procedures for the endurance of a cardiac valve prosthesis: stress/life and damage-tolerant analyses. J Biomech Eng 108:153–160
62. Newman Jr JC, Phillips EP, Swain MH (1997) Fatigue-life prediction methodology using small-crack theory. In: Center LR (ed.). Hampton
63. Suresh S (1998) Fatigue of materials, 2nd edn. Cambridge University Press
64. Paris P, Erdogan F (1963) A critical analysis of crack propagation laws. Trans ASME 85:528–534
65. Kitagawa H, Takahashi S (1976) Applicability of fracture mechanics to very small cracks or the cracks in the early stages. Second international conference on mechanical behavior of materials. American Society for Metals, Boston, pp 627–631
66. Pelton AR, Huang GH, Moine P, Sinclair R (2012) Effects of thermal cycling on microstructure and properties in Nitinol. Mater Sci Eng A 532:130–138
67. Simon T, Kröger A, Somsen C, Dlouhy A, Eggeler G (2009) On the multiplication of dislocations during martensitic transformations in NiTi shape memory alloys. Acta Mater 58(5):1850–1860
68. Norfleet DM, Sarosi PM, Manchiraju S, Wagner MFX, Uchic MD, Anderson PM, Mills MJ (2009) Transformation-induced plasticity during pseudoelastic deformation in Ni-Ti microcrystals. Acta Mater 57(12):3549–3561